

# Balmer jump temperature determination in a large sample of low-metallicity H II regions<sup>★,★★,★★★</sup>

N. G. Guseva<sup>1</sup>, Y. I. Izotov<sup>1</sup>, P. Papaderos<sup>2,3</sup>, and K. J. Fricke<sup>3</sup>

<sup>1</sup> Main Astronomical Observatory, Ukrainian National Academy of Sciences, Zabolotnoho 27, Kyiv 03680, Ukraine  
e-mail: guseva@mao.kiev.ua

<sup>2</sup> Instituto de Astrofísica de Andalucía, Apdo. 3004, 18080 Granada, Spain

<sup>3</sup> Institute for Astrophysics, Friedrich-Hund-Platz 1, 37077 Göttingen, Germany

Received 19 July 2006 / Accepted 21 December 2006

## ABSTRACT

**Aims.** Continuing the systematic determination of the electron temperature of H II regions using the Balmer and/or Paschen discontinuities by Guseva et al. (2006, ApJ, 644, 890) we focus here on 3.6 m ESO telescope observations of a large new sample of 69 H II regions in 45 blue compact dwarf (BCD) galaxies. This data set spans a wide range in metallicity ( $Z_{\odot}/60 \lesssim Z \lesssim Z_{\odot}/3$ ) and, combined with the sample of 47 H II regions from Guseva et al. (2006), yields the largest spectroscopic data set ever used to derive the electron temperature in the H<sup>+</sup> zone.

**Methods.** In the same way as in Guseva et al. (2006) we have used a Monte Carlo technique to vary free parameters and to calculate a series of model spectral energy distributions (SEDs) for each H II region. The electron temperature in the H<sup>+</sup> zones was derived from the best fitting synthetic and observed SEDs in the wavelength range ~3200–5100 Å, which includes the Balmer jump.

**Results.** On the base of the present large spectroscopic sample we find that in hot ( $T_e(\text{H}^+) \gtrsim 11\,000$  K) H II regions the temperature of the O<sup>2+</sup> zone, determined from doubly ionised oxygen forbidden lines, does not differ statistically from the temperature of the H<sup>+</sup> zone. Thus, we confirm and strengthen the finding by Guseva et al. (2006). We emphasize that due to a number of modelling assumptions and the observational uncertainties for individual objects, only a large, homogeneous sample, as the one used here, can enable a conclusive study of the relation between  $T_e(\text{H}^+)$  and  $T_e(\text{O III})$ .

**Key words.** galaxies: irregular – galaxies: starburst – galaxies: ISM – galaxies: abundances

## 1. Introduction

A long-standing problem in the study of H II regions is connected to the fact that the electron temperatures derived from the hydrogen Balmer and Paschen discontinuity or from the UV helium discontinuity are systematically lower than those derived from the collisionally excited optical [O III] lines which are most often used for the temperature determination (e.g. see review in O'Dell et al. 2003).

Electron temperature determinations based both on collisionally excited line diagnostics and on the Balmer and Paschen jumps have been mainly applied to planetary nebulae (PNe) (e.g. Liu et al. 2000; Luo et al. 2001; Ruiz et al. 2003; Zhang et al. 2004; Peimbert et al. 2004; Wesson et al. 2005) and to nearly solar-metallicity H II regions in the Milky Way and several nearby galaxies with relatively high metallicities of 1/3–1/10 solar (e.g. Peimbert & Torres-Peimbert 1992; Peimbert et al. 1993, 2000; Peimbert 2003; Esteban et al. 1998; García-Rojas et al. 2004, 2005, 2006; González-Delgado et al. 1994). A common result of these studies is that, generally,  $T_e(\text{H}^+)$  is lower than  $T_e(\text{O III})$ . Only recently Guseva et al. (2006) have derived the

electron temperature of a relatively large sample of low-metallicity H II regions using the Balmer and Paschen jumps.

Differences between  $T_e(\text{H}^+)$  and  $T_e(\text{O III})$  were first discussed by Peimbert (1967), who introduced a concept of temperature fluctuations in the nebulae. To quantify temperature fluctuations he used the parameter  $t^2$ , the mean square temperature variation. It was shown in many studies of planetary nebulae and H II regions (e.g. Peimbert et al. 1995; Esteban et al. 1998, 1999, 2002; Liu et al. 2000, 2001) that the heavy element abundances derived from the recombination lines and from the collisionally excited lines are consistent if  $t^2$  is in the range 0.02–0.10. On the other hand, typical values of  $t^2$  for photoionization models of chemically and spatially homogeneous nebulae are significantly lower,  $t^2 = 0.00$ –0.02 (e.g. Kingdon & Ferland 1995; Pérez 1997).

In recent years point-to-point measurements of the electron temperature fluctuations have been done in several PNe and H II regions (Liu 1998; Rubin et al. 2002; Krabbe & Copetti 2005; Rubin et al. 2003; O'Dell et al. 2003). Only low amplitude temperature variations were found across the nebulae. This is probably because the projected parameter  $t_s^2$  derived in the point-to-point measurements of the electron temperature is different from the total parameter  $t^2$ . Copetti (2006) has shown that  $t_s^2$  gives only a low limit of  $t^2$ . Additionally, there are many difficulties to obtain the temperature maps of the whole nebulae when images and spectra obtained with different space-born and ground-based telescopes are combined (Luridiana et al. 2003a).

\* Based on observations collected at the European Southern Observatory, Chile, ESO program 76.B-0739.

\*\* Table 1 and Fig. 3 are only available in electronic form at <http://www.aanda.org>

\*\*\* Tables 3 and 4 are only available in electronic form at the CDS via anonymous ftp to [cdsarc.u-strasbg.fr](http://cdsarc.u-strasbg.fr) (130.79.128.5) or via <http://cdsweb.u-strasbg.fr/cgi-bin/qcat?J/A+A/464/885>

Thus, the observational data for PNe and H II regions with relatively low electron temperatures  $\leq 11\,000$  K certainly show systematic differences between the temperatures obtained from the collisionally excited lines and from the Balmer and Paschen jumps (see Fig. 12 in Guseva et al. 2006, for the data collected from literature). On the other hand, no significant differences between  $T_e(\text{H}^+)$  and  $T_e(\text{O III})$  were found for the higher-temperature H II regions (Guseva et al. 2006). This conclusion is in agreement with the results obtained by Peimbert et al. (2002), who compared  $T_e(\text{O III})$  and the electron temperature  $T_e(\text{He}^+)$  in the  $\text{He}^+$  zone. Adopting  $t^2 = 0.01\text{--}0.04$ , these authors found the temperature differences of (1–3)% in H II regions with  $T_e(\text{O III}) = 20\,000$  K and of (3–12)% in H II regions with  $T_e(\text{O III}) = 10\,000$  K. As  $T_e(\text{He}^+) < T_e(\text{H}^+)$  in PNe (Zhang et al. 2005) and  $T_e(\text{He}^+) \approx T_e(\text{H}^+)$  in H II regions (García-Rojas et al. 2005), the differences between  $T_e(\text{O III})$  and  $T_e(\text{H}^+)$  are expected to be not greater than (1–3)% in H II regions with the temperatures  $T_e(\text{O III}) \sim 20\,000$  K.

Different mechanisms are proposed to explain the observational differences in  $T_e$ . In particular, density and chemical abundance inhomogeneities, ionization of nebulae by low-energy cosmic rays are considered (e.g. Torres-Peimbert et al. 1990; Viegas & Clegg 1994; Liu et al. 2000; Tsamis et al. 2004; Tsamis & Péquignot 2005; Giammanco & Beckman 2005). However, no definite conclusions have been made concerning the main mechanism for these differences.

The knowledge of differences in  $T_e$  is important for the element abundance determination. The heavy element abundances are usually derived assuming that the temperature of the  $\text{H}^+$  zone is equal to the temperature of the  $\text{O}^{2+}$  zone. If instead,  $T_e(\text{H}^+)$  is smaller than  $T_e(\text{O III})$ , then the heavy element abundances would be increased. For the determination of the primordial He abundance from spectra of low-metallicity BCDs (e.g. Izotov & Thuan 2004) the knowledge of the temperature structure of a H II region is especially important because the high precision of 1–2% is required for the He abundance. Thus to estimate the systematic error of the primordial He abundance it is crucial to investigate whether temperature differences are as important in low-metallicity BCDs as they are in high-metallicity H II regions and PNe.

Guseva et al. (2006) have determined the electron temperature of  $\text{H}^+$  zones from the Balmer jump in 23 H II regions and from the Paschen jump in 24 H II regions in the metallicity range from 1/3 to 1/60 of solar, based, respectively, on Multiple Mirror Telescope (MMT) and Sloan Digital Sky Survey (SDSS) data. They used Monte Carlo simulations, varying the electron temperature in the  $\text{H}^+$  zone, the extinction of the ionised gas and that of the stellar population, the relative contribution of the ionised gas to the total emission and the star formation history to fit the spectral energy distribution (SED) of the galaxies in the large wavelength range, which includes the Balmer and Paschen discontinuities. The best sets of free parameters have been obtained from the minimization of the deviations between observed and modelled SEDs. It was found that the temperatures  $T_e(\text{O III})$  of the  $\text{O}^{2+}$  zones determined from the nebular to auroral line flux ratio of doubly ionised oxygen  $[\text{O III}] \lambda(4959+5007)/\lambda 4363$  do not differ, in a statistical sense, from the temperatures  $T_e(\text{H}^+)$  of the  $\text{H}^+$  zones determined from Balmer and Paschen jumps. On the other hand, Guseva et al. (2006) have emphasized that, due to large observational uncertainties and modelling assumptions for individual objects, only a statistical study of a large sample of H II regions can allow for definite conclusions.

Therefore in order to study the  $T_e(\text{O III})$  vs.  $T_e(\text{H}^+)$  relation over a large metallicity range, between  $Z_{\odot}/60$  and  $Z_{\odot}/3$ , and with

much improved statistics, we took new spectra of H II regions with the 3.6 m ESO telescope. These data are combined with the ones obtained by Guseva et al. (2006).

In Sect. 2, we describe the observations and data reduction of the new spectroscopic data. In Sect. 3 we compare  $T_e(\text{H}^+)$  and  $T_e(\text{O III})$  for the new BCD sample and those from literature. Our conclusions are summarized in Sect. 4.

## 2. Observations and data reduction

The sample observed with the 3.6 m ESO telescope consists of 69 low-metallicity H II regions in 45 BCDs. They were selected mainly from the literature. Particularly, two galaxies were selected from the Data Release 2 of the Six-Degree Field Galaxy Redshift Survey (6dFGRS) (Jones et al. 2005) and eighteen galaxies were selected from the Data Release 4 of the Sloan Digital Sky Survey (SDSS) (Adelman-McCarthy et al. 2006). The BCDs were chosen to span a large range of oxygen abundance, from about 1/60 to about 1/3 that of the Sun. Thus, we can study the dependence of temperature variations with metallicity. Since the electron temperature of a H II region depends on its metallicity, H II regions in our BCD sample span also a large range of electron temperatures. The equivalent width of the  $\text{H}\beta$  line,  $EW(\text{H}\beta)$ , is a measure of the relative contribution of the ionised gas emission to the total light. The selected galaxies cover a large range of  $EW(\text{H}\beta)$  from 10 Å to 382 Å.

All spectra were obtained with the EFOSC2 (ESO Faint Object Spectrograph and Camera) mounted at the 3.6 m ESO telescope at La Silla in two observing runs, the first one, during April 11–14, 2005 and the second one, during October 7–9, 2005. The observing conditions were photometric during all nights. For the spring observations we used the grism #14 and the grating 600 gr/mm. The long slit with  $1'' \times 300''$  was centered on the brightest part of each galaxy. The above instrumental setup gave a wavelength coverage of  $\lambda\lambda 3200\text{--}5083$ , a spectral resolution of  $\sim 6.2$  Å (FWHM) and a spatial scale of  $0''.314 \text{ pixel}^{-1}$  along the slit for the used  $2 \times 2$  pixel binning.

During the fall observations the grism #07 and the grating 600 gr/mm were used, resulting in a wavelength coverage of  $\lambda\lambda 3250\text{--}5200$ . These observations were carried out with a  $1''.2 \times 300''$  slit centered on the brightest part of each galaxy. The spectral resolution and spatial scale along this slit were  $\sim 6.2$  Å (FWHM) and  $0''.157 \text{ pixel}^{-1}$ , respectively.

Our sample galaxies were mostly observed at low airmass  $< 1.2$ . Spectroscopic observations at a higher airmass were carried out along the parallactic angle. Thus, no corrections for atmospheric refraction have been applied. The total exposure time of typically 40–60 min per galaxy was split up into 2–3 subexposures to allow for a more efficient rejection of cosmic ray hits. Three spectrophotometric standard stars were observed during each night for flux calibration. The journal of the observations is given in Table 1.

The data reduction was carried out with the IRAF<sup>1</sup> software package. This includes bias subtraction, flat-field correction, cosmic-ray removal, wavelength calibration, night sky background subtraction, correction for atmospheric extinction and absolute flux calibration of the two-dimensional spectrum. For

<sup>1</sup> IRAF is the Image Reduction and Analysis Facility distributed by the National Optical Astronomy Observatory, which is operated by the Association of Universities for Research in Astronomy (AURA) under cooperative agreement with the National Science Foundation (NSF).

each night the sensitivity curve was derived from averaging of three standard stars.

One-dimensional spectra of the bright H II regions in each galaxy were corrected for interstellar extinction using the reddening curve by Whitford (1958) and for redshift, derived from the observed wavelengths of the emission lines. Redshift-corrected spectra are shown in Fig. 3.

Emission line fluxes were measured using Gaussian profile fitting. The errors of the line flux measurements were calculated from the photon statistics of non-flux-calibrated spectra. They have been propagated in the calculations of the elemental abundance errors. The observed relative emission line fluxes  $F(\lambda)/F(\text{H}\beta)$  and fluxes  $I(\lambda)/I(\text{H}\beta)$  corrected for interstellar extinction and underlying stellar absorption, equivalent widths  $EW$ s of emission lines, extinction coefficients  $C(\text{H}\beta)$ , observed  $\text{H}\beta$  fluxes  $F(\text{H}\beta)$ , and equivalent widths of the hydrogen absorption lines are listed in Table 3. Not all galaxies observed with the 3.6 m telescope are included in Table 3 but all of them are used in the subsequent analysis. We excluded from Table 3 eight H II regions with an oxygen abundance of  $12 + \log \text{O}/\text{H} \leq 7.6$ . The emission line fluxes, electron temperatures, ionic and total element abundances for these H II regions are presented in Papaderos et al. (2006b, in preparation), as part of a detailed spectroscopic and photometric study of extremely metal-deficient star-forming galaxies. We neither include in Table 3 the two extremely metal-poor emission-line galaxies SDSS J2104–0035 and J0113+0052 discovered in SDSS. All observational data for these galaxies were published by Izotov et al. (2006a). Finally, Table 3 does not include the extremely metal-deficient BCDs SBS 0335–052W and SBS 0335–052E. A spectroscopic study of these two systems is presented in Papaderos et al. (2006a).

### 3. Results

#### 3.1. Electron temperature $T_e(\text{O III})$ and element abundances

The electron temperature  $T_e$ , ionic and total heavy element abundances were derived following Izotov et al. (2006b). In particular, for the  $\text{O}^{2+}$  and  $\text{Ne}^{2+}$  ions we adopt the temperature  $T_e(\text{O III})$  derived from the  $[\text{O III}] \lambda 4363/(\lambda 4959 + \lambda 5007)$  emission line ratio. The  $\text{O}^+$  and  $\text{Fe}^{++}$  abundances were derived with the temperature  $T_e(\text{O II})$ . The latter was obtained from the relation between  $T_e(\text{O III})$  and  $T_e(\text{O II})$  of Izotov et al. (2006b). The 3.6 m spectra covered only the blue wavelength region, so that the  $[\text{S II}] \lambda 6717, 6731$  emission lines can not be used for the electron number density determination. Therefore we have adopted  $N_e = 100 \text{ cm}^{-3}$ . The electron temperatures  $T_e(\text{O III})$  and  $T_e(\text{O II})$  for the high- and low-ionisation zones in H II regions respectively, the ionisation correction factors ( $ICFs$ ) and the ionic and total heavy element abundances for oxygen, neon and iron are given in Table 4 excluding data for 16 H II regions published in the papers by Izotov et al. (2006a); Papaderos et al. (2006a,b).

Relevant parameters to the purpose of the paper such as the equivalent width  $EW(\text{H}\beta)$  of the  $\text{H}\beta$  emission line, the electron temperature  $T_e(\text{O III})$  of the  $\text{O}^{2+}$  zone, the electron temperature  $T_e(\text{H}^+)$  of the  $\text{H}^+$  zone, the oxygen abundance  $12 + \log \text{O}/\text{H}$  and the extinction coefficient  $C(\text{H}\beta)$ , obtained from the Balmer decrement, are collected in Table 2 for the entire sample of the 69 H II regions observed with the 3.6 m ESO telescope.

#### 3.2. Electron temperature $T_e(\text{H}^+)$

To derive the electron temperature  $T_e(\text{H}^+)$  we use the same method as that described in detail by Guseva et al. (2006). The method is based on the determination of the electron temperature  $T_e(\text{H}^+)$  of  $\text{H}^+$  zones by fitting a series of model SEDs to the observed SEDs and finding the best fits. Each fit is performed over the whole observed spectral range shortward of  $\sim \lambda(5100\text{--}5200) \text{ \AA}$ , which includes the Balmer jump region ( $\lambda 3646 \text{ \AA}$ ). Besides the electron temperature  $T_e(\text{H}^+)$  which controls the magnitude of the Balmer jump, the shape of the SED depends on several other parameters. As each SED is the sum of both stellar and ionised gas emission, its shape depends on the relative brightness of these two components. In BCDs, the contribution of the ionised gas emission can be very large. However, the  $EW$ s of hydrogen emission lines never attain the theoretical values for pure ionized gas emission. This implies a non-negligible contribution of stellar emission in all sample galaxies. We therefore parametrize the relative contribution of gaseous emission to the stellar one by the equivalent width  $EW(\text{H}\beta)$ .

The shape of the spectrum depends also on reddening. The extinction coefficient for the ionised gas  $C(\text{H}\beta)$  has been obtained from the observed hydrogen Balmer decrement. Here we assume that the differences between the observed and theoretical recombination hydrogen Balmer line ratios are only due to reddening and underlying stellar absorption. However, additional source of differences, collisional excitation of hydrogen lines, could play some role in the hot H II regions (Stasińska & Izotov 2003; Luridiana et al. 2003b). Collisional excitation may increase the flux of the  $\text{H}\alpha$  emission line by  $\lesssim 5\%$  above the recombination value. The effect is less important,  $\lesssim 2\%$ , for the  $\text{H}\beta$  emission line. We find that ignoring collisional excitation of hydrogen lines does not change significantly the derived  $T_e(\text{H}^+)$ . As the  $\text{H}\alpha$  line is not present in our spectra, we decreased by 2% the flux of  $\text{H}\beta$  line measured in spectra of several hottest H II regions from our sample. Such correction results in decreasing  $C(\text{H}\beta)$  by  $\sim 0.07$ . Then the derived  $T_e(\text{H}^+)$  is not changed more than by  $\sim 1\%$  as compared to the case with the measured flux of the  $\text{H}\beta$  line. Therefore, for the whole sample we decided not to take into account collisional excitation of hydrogen lines and use the  $C(\text{H}\beta)$  obtained from the measured hydrogen line fluxes. We have no direct observational constraint for the reddening for the stellar component, which could differ from  $C(\text{H}\beta)$ . Therefore, for simplicity, we adopt in calculations that both extinctions  $C(\text{H}\beta)_{\text{gas}}$  and  $C(\text{H}\beta)_{\text{stars}}$ , respectively for the ionised gas emission and the stellar component emission, are randomly varied in the narrow range around  $C(\text{H}\beta)$ . Finally, the SED depends on the star formation history of the BCD.

We have carried out a series of Monte Carlo simulations to reproduce the SED in each H II region of our sample. To calculate the contribution of stellar emission to the SEDs, we have adopted a grid of the Padua stellar evolution models by Girardi et al. (2000)<sup>2</sup> with heavy element mass fractions  $Z = 0.0001, 0.0004, 0.001, 0.004, 0.008$ . Using these data we have calculated with the package PEGASE.2 (Fioc & Rocca-Volmerange 1997) a grid of instantaneous burst SEDs in a wide range of ages, from 0.5 Myr to 15 Gyr. We have adopted a stellar initial mass function with a Salpeter slope, an upper mass limit of  $100 M_\odot$  and a lower mass limit of  $0.1 M_\odot$ . Following Guseva et al. (2006) we could approximate the star formation history in BCDs by two short bursts of different age but equal durations and with different strengths. The old stellar population is usually

<sup>2</sup> <http://pleiadi.pd.astro.it>

**Table 2.** Comparison of  $t_e(\text{O III})^a$  and  $t_e(\text{H}^+)^b$  for the sample galaxies.

Galaxy	$EW(\text{H}\beta)$	$t_e(\text{O III})$	$t_e(\text{H}^+)$	$12 + \log \text{O}/\text{H}$	$C(\text{H}\beta)^c$
SBS 0335-052E SE	382.	$1.98 \pm 0.05$	$1.90 \pm 0.10$	7.28	0.00
Pox 186	358.	$1.67 \pm 0.02$	$2.00 \pm 0.07$	7.75	0.08
HS 2236+1344a	343.	$2.05 \pm 0.02$	$1.96 \pm 0.06$	7.49	0.14
UM 461a	335.	$1.66 \pm 0.02$	$1.77 \pm 0.32$	7.76	0.22
J 104457.80+035313.1a	318.	$1.96 \pm 0.02$	$1.91 \pm 0.08$	7.44	0.31
Tol 1214-277	314.	$2.04 \pm 0.03$	$1.92 \pm 0.06$	7.50	0.14
UM 570	310.	$1.83 \pm 0.02$	$1.83 \pm 0.13$	7.72	0.14
CGCG 032-017	308.	$1.38 \pm 0.01$	$1.48 \pm 0.21$	8.09	0.27
Pox 108	306.	$1.31 \pm 0.02$	$1.31 \pm 0.17$	8.11	0.08
UM 559	306.	$1.60 \pm 0.02$	$1.55 \pm 0.12$	7.72	0.06
SBS 0335-052E #7	299.	$1.97 \pm 0.06$	$1.91 \pm 0.06$	7.21	0.14
UM 442	289.	$1.30 \pm 0.01$	$1.29 \pm 0.09$	8.10	0.14
Mrk 1329	288.	$1.05 \pm 0.01$	$1.26 \pm 0.06$	8.33	0.03
Mrk 1236a	283.	$1.21 \pm 0.01$	$1.30 \pm 0.08$	8.17	0.14
Tol 2146-391	277.	$1.63 \pm 0.02$	$1.59 \pm 0.32$	7.78	0.18
CGCG 007-025a	274.	$1.58 \pm 0.02$	$1.83 \pm 0.27$	7.81	0.20
HS 2134+0400	262.	$2.02 \pm 0.04$	$1.86 \pm 0.20$	7.41	0.25
J 001434.98-004352.0	260.	$1.39 \pm 0.04$	$1.31 \pm 0.28$	7.97	0.12
J 232420.34-000625.0	249.	$1.41 \pm 0.01$	$1.55 \pm 0.22$	7.95	0.20
SBS 0335-052E #3b	249.	$2.04 \pm 0.03$	$2.07 \pm 0.22$	7.31	0.45
J 125305.96-031258.9	248.	$1.38 \pm 0.01$	$1.34 \pm 0.21$	8.01	0.36
J 120122.30+021108.3	248.	$1.81 \pm 0.03$	$1.70 \pm 0.27$	7.49	0.09
SBS 0335-052E #3a	246.	$2.02 \pm 0.03$	$2.05 \pm 0.22$	7.31	0.43
Tol 65a	244.	$1.76 \pm 0.02$	$1.83 \pm 0.17$	7.54	0.10
UM311	243.	$0.99 \pm 0.01$	$1.00 \pm 0.04$	8.36	0.22
J 130432.27-033322.1	233.	$1.08 \pm 0.01$	$1.20 \pm 0.08$	8.24	0.12
J 024815.95-081716.5a	233.	$1.32 \pm 0.01$	$1.13 \pm 0.19$	8.04	0.04
Pox 4a	220.	$1.39 \pm 0.01$	$1.11 \pm 0.23$	8.01	0.08
Pox 120a	215.	$1.53 \pm 0.01$	$1.76 \pm 0.22$	7.88	0.21
HS 2236+1344b	215.	$1.86 \pm 0.02$	$1.80 \pm 0.10$	7.58	0.22
CGCG 007-025c	214.	$1.56 \pm 0.02$	$1.49 \pm 0.25$	7.78	0.02
UM 462a	212.	$1.39 \pm 0.01$	$1.45 \pm 0.22$	8.00	0.52
J 230210.00+004938.8	212.	$1.80 \pm 0.03$	$1.91 \pm 0.09$	7.63	0.00
Tol 2138-405	208.	$1.39 \pm 0.02$	$1.08 \pm 0.12$	7.99	0.39
J 210455.31-003522.2N	203.	$2.01 \pm 0.08$	$1.87 \pm 0.18$	7.26	0.00
J 011340.44+005239.1	193.	$2.29 \pm 0.30$	$2.55 \pm 0.04$	7.17	0.00
J 013352.56+134209.3	178.	$1.74 \pm 0.02$	$1.62 \pm 0.33$	7.56	0.04
Pox 4b	177.	$1.43 \pm 0.01$	$1.51 \pm 0.18$	7.87	0.00
IC 4662a	172.	$1.27 \pm 0.01$	$1.34 \pm 0.19$	8.09	0.44
J 143053.50+002746.3	168.	$1.30 \pm 0.01$	$1.21 \pm 0.15$	8.07	0.15
IC 4662c	166.	$1.25 \pm 0.01$	$1.25 \pm 0.14$	8.16	0.33
Pox 120b	158.	$1.37 \pm 0.02$	$1.18 \pm 0.20$	7.99	0.14
g2252292-171050	158.	$1.59 \pm 0.02$	$1.74 \pm 0.24$	7.82	0.10
UM 461b	147.	$1.58 \pm 0.02$	$1.79 \pm 0.23$	7.77	0.18
Mrk 1236c	147.	$1.22 \pm 0.04$	$0.98 \pm 0.03$	8.05	0.00
J 144805.36-011057.7	146.	$1.39 \pm 0.01$	$1.44 \pm 0.24$	8.00	0.21
IC 4662b	140.	$1.27 \pm 0.01$	$1.32 \pm 0.07$	8.10	0.14
J 223036.79-000636.9	133.	$1.71 \pm 0.03$	$1.86 \pm 0.30$	7.64	0.34
Pox 105	131.	$1.53 \pm 0.02$	$1.49 \pm 0.27$	7.85	0.04
UM 462d	130.	$1.45 \pm 0.03$	$1.52 \pm 0.26$	7.86	0.23
UM 462c	127.	$1.48 \pm 0.02$	$1.11 \pm 0.15$	7.88	0.00
J 024815.95-081716.5b	125.	$1.35 \pm 0.04$	$1.36 \pm 0.18$	7.99	0.00
CGCG 007-025b	122.	$1.58 \pm 0.02$	$1.67 \pm 0.19$	7.75	0.06
J 162410.12-002202.5	122.	$1.20 \pm 0.01$	$1.21 \pm 0.15$	8.16	0.16
UM 462e	112.	$1.59 \pm 0.05$	$1.67 \pm 0.26$	7.77	0.00
J 013452.00-003854.4	111.	$1.49 \pm 0.15$	$1.53 \pm 0.26$	7.85	0.16
SBS 0335-052W	109.	$1.97 \pm 0.25$	$2.01 \pm 0.25$	7.13	0.02
Tol 65b	96.	$1.69 \pm 0.04$	$1.74 \pm 0.31$	7.59	0.14
SBS 0335-052E #4,5	89.	$2.11 \pm 0.04$	$1.90 \pm 0.13$	7.27	0.26

approximated by continuous star formation (e.g. Guseva et al. 2001, 2003a–c). However, the contribution of the old stellar population to the light of the bright H II regions considered in this paper is always small, not exceeding a few percent in the optical range. Therefore, the approximation of a short burst for

the old stellar population is acceptable for our modelling, as it was shown by Guseva et al. (2006). The contribution of gaseous emission to the total emission is scaled by the ratio of the observed equivalent width of the H $\beta$  emission line to the  $EW(\text{H}\beta)$  expected for pure gaseous emission. The gaseous continuum

Table 2. continued.

Galaxy	$EW(H\beta)$	$t_e(O III)$	$t_e(H^+)$	$12 + \log O/H$	$C(H\beta)^c$
UM 462b	85.	$1.42 \pm 0.02$	$1.44 \pm 0.15$	7.92	0.21
CGCG 007-025d	69.	$1.68 \pm 0.04$	$1.72 \pm 0.27$	7.65	0.00
ESO 338-IG04	59.	$1.46 \pm 0.02$	$1.44 \pm 0.27$	7.90	0.02
Mrk 1236b	56.	$1.17 \pm 0.02$	$1.14 \pm 0.22$	8.12	0.07
J 141454.13-020822.9	48.	$1.89 \pm 0.01$	$1.98 \pm 0.23$	7.32	0.08
IC 4662d	44.	$1.25 \pm 0.02$	$1.12 \pm 0.28$	8.07	0.14
J 010746.56+010352.0	40.	$1.56 \pm 0.23$	$1.57 \pm 0.25$	7.68	0.12
g0405204-364859	23.	$2.08 \pm 0.25$	$1.95 \pm 0.21$	7.34	0.02
J 104457.80+035313.1b	20.	$1.94 \pm 0.21$	$1.81 \pm 0.32$	7.45	0.14
IC 4662e	10.	$1.31 \pm 0.01$	$1.30 \pm 0.23$	8.08	0.06

<sup>a</sup>  $t_e(O III) = T_e(O III)/10\,000$  K, derived from the  $[O III] \lambda(4959+5007)/\lambda 4363$  emission line ratio.

<sup>b</sup>  $t_e(H^+) = T_e(H^+)/10\,000$ , derived as the weighted mean temperature from the 10 best fits of the SED.

<sup>c</sup> Extinction coefficient is derived from observed hydrogen Balmer decrement.

emission is calculated following Aller (1984) and includes hydrogen and helium free-bound, free-free, and two-photon emission. In our models it is always calculated with the electron temperature  $T_e(H^+)$  and with the He/H abundance ratio derived from the H II region spectrum. The observed emission lines corrected for reddening and scaled using the absolute flux of the  $H\beta$  emission line were added to the calculated gaseous continuum.

Given that  $T_e(H^+)$  is not necessarily equal to  $T_e(O III)$ , we chose to vary it in the range  $(0.7-1.3) \times T_e(O III)$ . We adopt for the range of the allowed  $EW(H\beta)$  values between 0.95 and 1.05 times its nominal value. As for the extinction, we allow both  $C(H\beta)_{stars}$  and  $C(H\beta)_{gas}$  to vary in the range of  $(0.8-1.2)$  of  $C(H\beta)$ , obtained from the Balmer decrement.

We assume that the young stellar population was formed in a recent burst of star formation with an age  $t(\text{young})$  between 0.3 and 10 Myr. For the age of the older stars  $t(\text{old})$  we adopt values between 10 Myr and 15 Gyr. The contribution of each burst to the SED is defined by the ratio of the masses of stellar populations formed respectively in the old and young bursts,  $b = M(\text{old})/M(\text{young})$ , which we vary between 0.01 and 100. For each H II region we computed a series of synthetic SEDs using a grid of Padua models with the heavy element mass fraction, that is closest to the heavy element mass fraction of the ionised gas. We run  $10^5$  Monte Carlo models for each H II region varying simultaneously  $t(\text{young})$ ,  $t(\text{old})$ ,  $b$ ,  $T_e(H^+)$ ,  $C(H\beta)_{gas}$  and  $C(H\beta)_{stars}$ . The first four parameters are used to calculate the model  $EW(H\beta)$ . Only those solutions were further considered for the SED fitting in which the modelled  $EW(H\beta)$  falls in the range 0.95–1.05 of the observed one. Typically, the number of such solutions is  $\sim 10-100$  times less than the total of  $10^5$  simulations.

In the same way as in Guseva et al. (2006) we used the  $\sigma$  statistic to quantify the goodness of each model's fit to the observed SED. For each Monte Carlo realization we computed a mean deviation  $\sigma$  between the observed and modelled spectra. We calculate in each spectrum the root mean square deviation  $\sigma_j$  for each of the five continuum regions selected to be devoid of line emission and absorption, as  $\sigma_j = \sqrt{\sum_{i=1}^{N_j} (f_{obs}^i - f_{mod}^i)^2 / N_j}$ , where  $N_j$  is the number of the points in each particular spectral interval. Then  $\sigma = \sum \sigma_j / 5$ .

As shown in Fig. 2a, for all Monte Carlo realizations the age  $t(\text{old})$  and  $t(\text{young})$  and mass ratio  $b$  of the old and young stellar populations, and the electron temperature  $T_e(H^+)$  in the  $H^+$  zone span a wide range. However, if only solutions with the lowest  $\sigma$ s are taken into account then the range of the electron temperature in the  $H^+$  zone for many H II regions from our sample is considerably narrowed (Figs. 2b and c). On the other

hand, for some H II regions the minimum in the distribution of  $\sigma$  is not sharp and even two minima in the distribution of  $\sigma$  are obtained with significantly different  $T_e(H^+)$  (see also Fig. 9 in Guseva et al. 2006). The  $T_e(H^+)$  of each H II region is derived as the average of the electron temperatures obtained for several best-fitting SEDs. We also derive the dispersion around the average  $T_e(H^+)$  of the electron temperatures obtained from the same best-fitting SEDs. Then small dispersions correspond to sharp single minima in the distributions of  $\sigma$ . We have checked how the derived  $T_e(H^+)$  does depend on the exact number of best solutions we choose to average. No systematic differences were found when the number of best fits varies between a few and a couple of ten (Guseva et al. 2006). Hence, we adopt for  $t_e(H^+) = 10^{-4} T_e(H^+)$  the mean of the 10 best-fitting solutions weighted by  $\sigma$ .

We note that the bimodal  $\sigma$  distribution for some H II regions does not allow to derive a unique  $T_e(H^+)$  in those objects. The average  $T_e(H^+)$  of the 10 best-fitting solutions for these H II regions can significantly differ from the actual one. On the other hand, the dispersion of the average  $T_e(H^+)$ s in H II regions with the bimodal  $\sigma$  distribution is large reflecting the uncertainties of the temperature determination. Therefore, in the following discussion we will use different samples: the total sample (Fig. 4a) and the samples with the sharp minimum in the  $\sigma$  distribution (Figs. 4b,c).

### 3.3. Comparison of $t_e(H^+)$ and $t_e(O III)$

Figure 3 shows by a thick solid line the best-fit SED (SED with the smallest  $\sigma$ ) superimposed on the redshift- and extinction-corrected observed spectrum of each H II region in the sample, including the H II regions discussed by Izotov et al. (2006a) and Papaderos et al. (2006a,b).

The galaxies are arranged in order of decreasing  $H\beta$  equivalent width, i.e. in order of decreasing contribution of gaseous emission relative to stellar emission. It is seen that, in every case, the model SED fits well the observed one over the whole spectral range, including the Balmer jump region. The separate contributions from the stellar and ionised gas components are shown by thin solid lines.

In Fig. 4a we compare  $t_e(H^+)$  and  $t_e(O III) = 10^{-4} T_e(O III)$ . The 3.6 m data for the sample of 69 H II regions in 45 BCDs are shown by large filled circles and, in the case of Pox 186 and UM 462c, by squares. The electron temperature  $t_e(H^+)$  for each galaxy is the mean of the temperatures derived from the 10 best Monte Carlo realizations weighted by their  $\sigma$ s (Table 2). Error

bars are the root mean square temperature deviations from the mean of the 10 best Monte Carlo simulations. The dashed line denotes equal temperatures, while the solid line is a linear regression  $t_e(\text{H}^+) = 1.078 \times t_e(\text{O III}) - 0.054$  obtained with the likelihood method (Press et al. 1992) for all 116 H II regions that takes into account errors in  $t_e(\text{H}^+)$  and  $t_e(\text{O III})$  in each object. Dotted lines illustrate  $1\sigma$  deviations of the sample H II regions from the linear regression. The linear regression is almost not changed if the outlying object with the highest electron temperature  $t_e(\text{O III})$  is excluded. It is seen from Fig. 4a that the linear regression (solid line) is slightly different from the line of equal temperatures (dashed line) because of the small dispersion of  $t_e(\text{H}^+)$  for the H II region Mrk 71 No. 1 (Guseva et al. 2006) and, therefore, its large weight in the linear regression determination. On the other hand, if equal dispersions of  $t_e(\text{H}^+)$  are adopted for all H II regions, the linear regression deviates very little from the line of equal temperatures. All these differences are smaller than the  $1\sigma$  deviations of H II regions from the linear regression (dotted lines). Therefore, we conclude that no systematic difference between  $t_e(\text{O III})$  and  $t_e(\text{H}^+)$  is evident from Fig. 4a.

Our 3.6 m observations in Fig. 4a are supplemented by the data from previous studies. The results of  $t_e(\text{H}^+)$  determination from Balmer jump for 23 low-metallicity H II regions (MMT data) and Paschen jump for 24 low-metallicity H II regions (SDSS data) from Guseva et al. (2006) are shown by large and small open circles respectively. In Fig. 4a we also plot some other data from the literature. By stars are shown the H II regions: M17 (Peimbert & Torres-Peimbert 1992), Orion nebula (Esteban et al. 1998), NGC 3576 (García-Rojas et al. 2004), S 310 (García-Rojas et al. 2004, 2006) in the Galaxy; 30 Dor in Large Magellanic Cloud (Peimbert 2003); NGC 346 in Small Magellanic Cloud (Peimbert et al. 2000); and H II regions A and B in the BCD Mrk 71 (González-Delgado et al. 1994). By dots in Fig. 4a we plot the data for 58 Galactic PNe by Liu et al. (2004), Zhang et al. (2004), Wesson et al. (2005) and Krabbe & Copetti (2005). The data collected from literature extend the  $t_e(\text{H}^+) - t_e(\text{O III})$  relation to lower temperatures.

In Fig. 4b are shown only 41 H II regions with small dispersions of  $t_e(\text{H}^+)$  ( $\sigma[t_e(\text{H}^+)]/t_e(\text{H}^+) < 0.1$ ) for 3.6 m data (present paper) and for data from Guseva et al. (2006) (MMT and SDSS data). These data are fitted by a linear regression  $t_e(\text{H}^+) = 1.085 \times t_e(\text{O III}) - 0.050$  (solid line) that is very similar to the linear regression obtained for the whole sample of 116 H II regions. If the outlying point with the highest  $t_e(\text{O III})$  is excluded the linear regression is almost not changed. Thus, from the analysis of the subsample of H II regions with sharpest minima in the  $\sigma$  distribution we reach the same conclusion as that based on the total sample: there is no significant differences between  $t_e(\text{H}^+)$  and  $t_e(\text{O III})$ . However, we cannot exclude small differences of  $\leq 1000$  K, corresponding to the temperature fluctuation parameter  $t^2 \leq 0.02$ .

Special emphasis was given to the analysis of a few H II regions which are most deviant from the line of equal electron temperatures in Fig. 4a. Two of these H II regions, UM 462c and Pox 186, are labeled in Fig. 4a. One of these sources, Pox 186, has been studied previously by Guseva et al. (2004). No H I 21 cm emission was detected in this galaxy. Its H II region is characterised by a very high  $\text{O}^{2+}/\text{O}^+$  abundance ratio of  $\sim 20$  and likely shows Ly $\alpha$  emission in the UV. These properties led Guseva et al. (2004) to conclude that the H II region in Pox 186 may be density-bounded. If this is indeed the case then  $EW(\text{H}\beta)$  does not measure the starburst age anymore. Its inclusion into our modelling procedure would then result in an incorrect

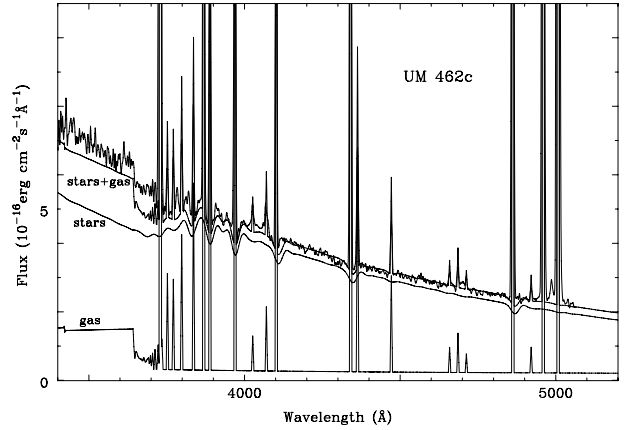


**Fig. 1.** Best fit model SED to the redshift- and extinction-corrected observed spectrum of UM 462c. The model SED is calculated assuming that the H II region is ionisation-bounded. It is seen that the red part of spectrum is fitted quite well whereas the modelled SED underestimates the flux shortward of the Balmer jump. This is likely due to the leakage of ionising photons from the H II region.

reproduction of the star formation history and the stellar SED. While this assumption is less critical in the case of Pox 186 because of the high  $EW(\text{H}\beta)$  and hence the dominant contribution of gaseous emission to the total emission of this system, it is important for the case of a H II region with lower  $EW(\text{H}\beta)$ , such as UM 462c. This is illustrated in Fig. 1 where we show the model SED which best fits the observed spectrum of UM 462c. It is seen that the ionisation-bounded model of the H II region fails to reproduce the observations regardless of the adopted synthetic SED. Specifically, the models underestimate the SED blueward of the Balmer jump, whereas redward of it they provide a satisfactory fit. The most likely reason for this discrepancy is leakage of ionising photons from the H II region.

The discrepancy between observed and modelled SEDs can be eliminated, however, assuming a H II region model with escaping Ly $\alpha$  photons, which implies a larger number of massive ionising stars than the number needed to account for the observed  $EW(\text{H}\beta)$  in the case of an ionisation-bounded H II region. Thus, Monte Carlo simulations assuming a H II region with escaping Ly $\alpha$  photons require a younger stellar population with a larger production rate of ionising photons, compared to models assuming an ionisation-bounded H II region. As a result the stellar SED blueward of the Balmer jump is actually larger than what fits to  $EW(\text{H}\beta)$  imply. In practice, in order to account for the fraction of photons escaping from the H II region we need to introduce an additional parameter  $f$ . Then, the modelled SED of the ionised gas emission and  $EW(\text{H}\beta)$  must be multiplied by a factor  $(1 - f)$  to match the observed ones.

In Fig. 4a we show by open squares the  $t_e(\text{H}^+)$  for Pox 186 and UM 462c obtained from the ionisation-bounded model and by filled squares the  $t_e(\text{H}^+)$  obtained from the model with escaping Ly $\alpha$  photons. It is seen that the  $t_e(\text{H}^+)$  obtained from the latter models for both H II regions (filled squares) are in better agreement with the data for other H II regions. This is also evident from Fig. 3 where we plot the best-fit SEDs obtained for these two systems from models with escaping Ly $\alpha$  photons. These SEDs reproduce quite well the observed spectra over their whole wavelength range, including the region blueward of the Balmer jump.

The leakage of Ly $\alpha$  photons could be present in other H II regions from our sample. This may introduce an additional source

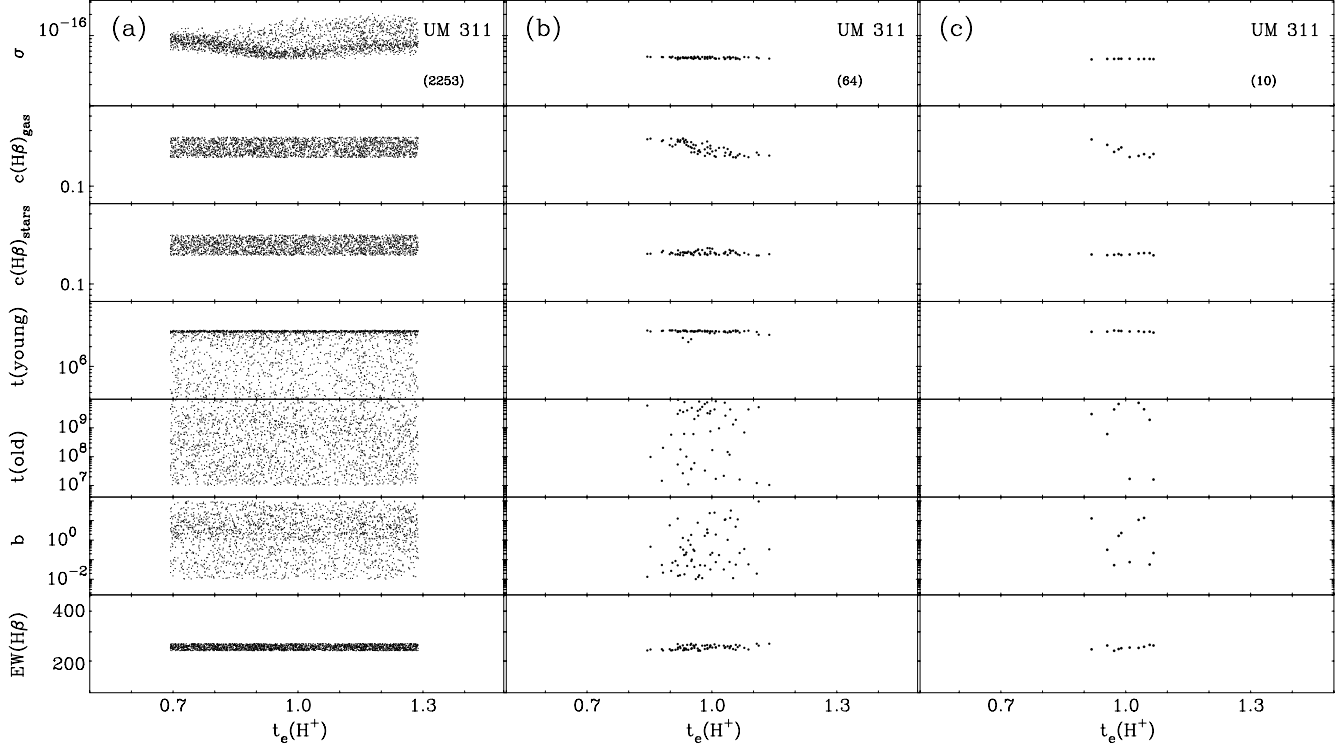


**Fig. 2.** **a)** Example of the parameter space explored with the Monte Carlo technique (2253 solutions out of  $10^5$  simulations) to fit the spectrum of the BCD UM 311. The parameters shown are the equivalent width of the  $H\beta$  emission line  $EW(H\beta)$ , the ages of the old and young stellar populations,  $t(\text{old})$  and  $t(\text{young})$ , the mass ratio  $b$  of the old-to-young stellar population, the extinction coefficient for the stellar emission  $C(H\beta)_{\text{stars}}$ , the extinction coefficient for the ionised gas  $C(H\beta)_{\text{gas}}$ , and the electron temperature  $t_e(H^+) = 10^{-4}T_e(H^+)$  in the  $H^+$  zone. The parameter  $\sigma$  is an estimator of the goodness of the fit. **b)** and **c)** are the same as **a)** except that only the 64 and 10 best Monte Carlo realizations are shown.

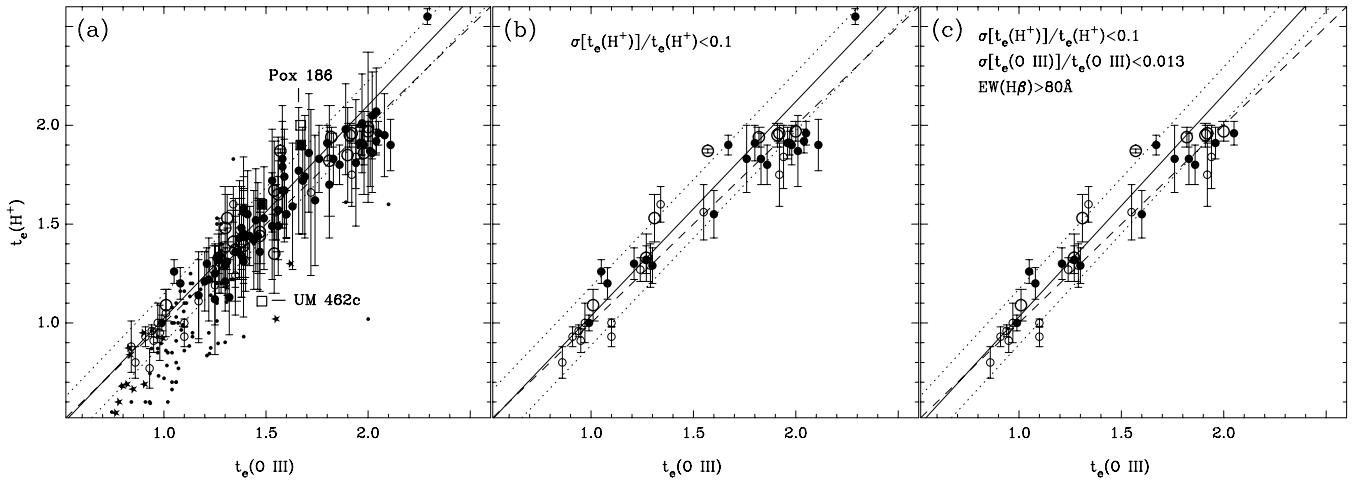


**Fig. 4.** **a)** Comparison of the  $t_e(H^+)$  derived from fitting the Balmer jump and the SED with the  $t_e(O\text{ III}) = 10^{-4}T_e(O\text{ III})$  derived from the nebular to auroral line flux ratio  $[O\text{ III}] \lambda(4959+5007)/\lambda 4363$ . In each panel, the dashed line denotes equal temperatures, the solid line is the linear regression obtained by the likelihood method (Press et al. 1992), dotted lines denote  $1\sigma$  dispersions of our sample H II regions around the regression line. Error bars are the root mean square temperature deviations from the mean of the 10 best Monte Carlo simulations. 3.6 m data are shown by large filled circles. Two objects, Pox 186 and UM 462c, which could not be fitted by ionisation-bounded model are denoted by squares. For each of these two galaxies we show by open squares the solutions from the ionisation-bounded model and by filled squares the solutions from the model with escaping Ly $\alpha$  photons. The derived  $t_e(H^+)$  from the Balmer jump in 23 low-metallicity H II regions (MMT data) and the Paschen jump in 24 low-metallicity H II regions (SDSS data) are shown by large and small open circles, respectively (Guseva et al. 2006). For comparison we have also plotted by dots in **a)** the data of Liu et al. (2004), Zhang et al. (2004), Wesson et al. (2005) and Krabbe & Copetti (2005) for 58 Galactic PNe. Stars show the data for H II regions from Esteban et al. (1998), García-Rojas et al. (2004, 2006), Peimbert & Torres-Peimbert (1992), Peimbert et al. (2000), Peimbert (2003) and González-Delgado et al. (1994). **b)** This panel is identical to panel **a)** except that only H II regions with small dispersions for  $t_e(H^+)$  ( $\sigma[t_e(H^+)/t_e(H^+)] < 0.1$ ) for 3.6 m data (present paper) and data from Guseva et al. (2006) (MMT and SDSS data) are shown. **c)** The same as in **a)** but only H II regions with large equivalent widths and small errors for  $t_e(H^+)$  and  $t_e(O\text{ III})$  are included ( $\sigma[t_e(H^+)/t_e(H^+)] < 0.1$ ;  $\sigma[t_e(O\text{ III})]/t_e(O\text{ III}) < 0.013$ ;  $EW(H\beta) > 80 \text{ \AA}$ ).

of uncertainties in the determination of  $t_e(\text{H}^+)$ . However, the fact that majority of H II regions are well fitted by the models with non-escaping Ly $\alpha$  photons suggests that in general  $f$  is small. Our conclusion is supported by multi-wave-band studies by Leitherer et al. (1995). They find that less than 3% of ionizing photons escape from local starburst galaxies. More recently, for several local starburst galaxies, Heckman et al. (2001) estimate  $f \lesssim 6\%$  and Bergvall et al. (2006) find  $f \sim 4\%–10\%$  for another local starburst. The direct detection of Lyman continuum emission from 14 high-redshift star-forming galaxies shows that only 2 of 14 studied galaxies have a significant emission below the Lyman limit (Shapley et al. 2006). Therefore, for all our H II regions except for Pox 186 and UM 462c we decided to apply the models with the smallest number of free parameters adopting  $f = 0$ .

Inspection of Fig. 4b also reveals that some of the H II regions from the 3.6 m data sample with the highest temperatures [ $t_e(\text{H}^+) \sim 1.9$  and  $t_e(\text{O III}) \gtrsim 2.0$ ] are offset from the linear regression and from the line of equal temperatures, at variance to H II regions with a lower  $t_e(\text{H}^+)$ . These offset galaxies are low-excitation H II regions with weak [O III] $\lambda 4363$  emission lines. Therefore, the determination of  $t_e(\text{O III})$  is more uncertain in those galaxies. Indeed, the number of deviant points from the line of equal temperatures are decreased if only galaxies with high equivalent widths of H $\beta$  ( $EW(\text{H}\beta) > 80 \text{ \AA}$ ) and small  $t_e(\text{O III})$  and  $t_e(\text{H}^+)$  errors are considered (Fig. 4c).

With the additional PNe data an interesting trend appears in Fig. 4a. While the PNe data scatters nicely on either side of the line of equal temperatures for  $t_e(\text{O III}) \gtrsim 1.1$ , just as the BCD data, the  $t_e(\text{H}^+) - t_e(\text{O III})$  relationship curves down for objects with  $t_e(\text{O III}) \lesssim 1.1$ , with  $t_e(\text{H}^+)$  being systematically lower than  $t_e(\text{O III})$ . There are several cool H II regions collected from literature and shown by stars, which also follow the trend delineated by PNe. All other H II regions with  $t_e > 1.0$  collected from literature do not deviate from line of equal temperatures, similar to the sample of 116 H II regions in 88 emission-line galaxies collected from 3.6 m, MMT and SDSS data.

Thus, we confirm the previous finding by Guseva et al. (2006) that the temperature of the O III zone is equal, within the errors, to the temperature of the H $^+$  zone in the H II regions with  $T_e(\text{H}^+) \gtrsim 11\,000 \text{ K}$ . We emphasize that, due to the large observational uncertainties for each individual object and a number of modelling assumptions, only a statistical study of a large, homogeneous sample of H II regions allows us to firmly establish the relation between  $T_e(\text{H}^+)$  and  $T_e(\text{O III})$ .

## 4. Conclusions

Based on 3.6 m ESO spectroscopic data, we have determined in this paper the temperatures of the H $^+$  zones in 69 H II regions of 45 blue compact dwarf (BCD) galaxies. Following the procedure of Guseva et al. (2006), we have used a Monte Carlo technique to vary free parameters and to calculate a series of model spectral energy distributions (SEDs). The electron temperature of H $^+$  zones were derived from best-fit SEDs to the observed spectra in the wavelength range  $\sim 3200–5100 \text{ \AA}$ , which includes the Balmer jump region. These new data are combined with a sample of 47 H II regions from Guseva et al. (2006) in order to study systematic trends in the electron temperature determination over a wide range in oxygen abundance ( $7.13 \leq 12 + \log(\text{O}/\text{H}) \leq 8.36$ ) and H $\beta$  equivalent width ( $10 \text{ \AA} \leq EW(\text{H}\beta) \leq 382 \text{ \AA}$ ). This is the largest spectroscopic sample of low-metallicity H II regions ever compiled in order to address the long-standing

question of how the electron temperature of H $^+$  zones is related to that derived from collisionally excited forbidden lines.

We conclude that in H II regions with an electron temperature  $T_e(\text{H}^+) \gtrsim 11\,000 \text{ K}$  the temperature of the O $^{2+}$  zone, determined from the nebular to auroral line flux ratio of doubly ionised oxygen [O III]  $\lambda(4959+5007)/\lambda 4363$  is, within the errors, equal to the temperature of the H $^+$  zone determined from fitting the SED including that in the Balmer jump wavelength region. However, we could not exclude small differences of  $\leq 1000 \text{ K}$  between  $T_e(\text{H}^+)$  and  $T_e(\text{O III})$  corresponding to the temperature fluctuations parameter  $t^2 \leq 0.02$ .

Consequently, temperature differences could not be of concern for the determination of the primordial He abundance, as it relies mainly on the hot low-metallicity H II regions. Thus, on the base of a new large sample of low-metallicity BCDs we confirm and strengthen the previous finding by Guseva et al. (2006), based on the analysis and modelling of the Balmer and Paschen jump in a smaller sample of low-metallicity H II regions.

We also identify and discuss cases of H II regions where ionisation-bounded models fail to fit the observed SEDs. Such models typically underestimate the object's SED blueward of the Balmer discontinuity. This can be, however, plausibly accounted for by photoionisation models allowing for the partial leakage of Ly $\alpha$  photons from a H II region.

*Acknowledgements.* Y.I.I. and N.G.G. thank the hospitality of the Institute for Astrophysics (Göttingen), and the support of the DFG grant No. 436 UKR 17/25/05. P.P. would like to thank Gaspare Lo Curto, Lorenzo Monaco, Carlos La Fuente, Eduardo Matamoros and the whole ESO staff at the La Silla Observatory for their support. All the authors acknowledge the work of the Sloan Digital Sky Survey (SDSS) team. Funding for the SDSS has been provided by the Alfred P. Sloan Foundation, the Participating Institutions, the National Aeronautics and Space Administration, the National Science Foundation, the US Department of Energy, the Japanese Monbukagakusho, and the Max Planck Society. The SDSS Web site is <http://www.sdss.org/>.

## References

- Adelman-McCarthy, J. K., Augüeros, M. A., Allam, S. S., et al. 2006, *ApJS*, 162, 38
- Aller, L. H. 1984, *Physics of Thermal Gaseous Nebulae* (Dordrecht: Reidel)
- Bergvall, N., Zackrisson, E., Andersson, B.-G., et al. 2006, *A&A*, 448, 513
- Copetti, M. V. F. 2006, *A&A*, 453, 943
- Esteban, C., Peimbert, M., Torres-Peimbert, S., & Escalante, V. 1998, *MNRAS*, 295, 301
- Esteban, C., Peimbert, M., Torres-Peimbert, S., García-Rojas, J., & Rodríguez, M. 1999, *ApJS*, 120, 113
- Esteban, C., Peimbert, M., Torres-Peimbert, S., & Rodríguez, M. 2002, *ApJ*, 581, 241
- Fioc, M., & Rocca-Volmerange, B. 1997, *A&A*, 326, 950
- García-Rojas, J., Esteban, C., Peimbert, M., et al. 2004, *ApJS*, 153, 501
- García-Rojas, J., Esteban, C., Peimbert, A., et al. 2005, *MNRAS*, 362, 301
- García-Rojas, J., Esteban, C., Peimbert, M., et al. 2006, *MNRAS*, 368, 253
- Giammanco, C., & Beckman, J. E. 2005, *A&A*, 437, L11
- Girardi, L., Bressan, A., Bertelli, G., & Chiosi, C. 2000, *A&AS*, 141, 371
- González-Delgado, R. M., Perez, E., Tenorio-Tagle, G., et al. 1994, *ApJ*, 437, 239
- Guseva, N. G., Izotov, Y. I., Papaderos, P., et al. 2001, *A&A*, 378, 756
- Guseva, N. G., Papaderos, P., Izotov, Y. I., et al. 2003a, *A&A*, 407, 75
- Guseva, N. G., Papaderos, P., Izotov, Y. I., et al. 2003b, *A&A*, 407, 91
- Guseva, N. G., Papaderos, P., Izotov, Y. I., et al. 2003c, *A&A*, 407, 105
- Guseva, N. G., Papaderos, P., Izotov, Y. I., Noeske, K. G., & Fricke, K. J. 2004, *A&A*, 421, 519
- Guseva, N. G., Izotov, Y. I., & Thuan, T. X. 2006, *ApJ*, 644, 890
- Heckman, T. M., Sembach, K. R., Meurer, G. R., et al. 2001, *ApJ*, 558, 56
- Izotov, Y. I., & Thuan, T. X. 2004, *ApJ*, 602, 200
- Izotov, Y. I., Papaderos, P., Guseva, N. G., Fricke, K. J., & Thuan, T. X. 2006a, *A&A*, 454, 137
- Izotov, Y. I., Stasińska, G., Meynet, G., Guseva, N. G., & Thuan, T. X. 2006b, *A&A*, 448, 955

- Jones, D. H., Saunders, W., Read, M. A., & Colless, M. 2005, *PASA*, 22, 277
- Kingdon, J. B., & Ferland, G. J. 1995, *ApJ*, 450, 691
- Krabbe, A. C., & Copetti, V. F. 2005, *A&A*, 443, 981
- Leitherer, C., Ferguson, H. C., Heckman, T. M., & Lowenthal, J. D. 1995, *ApJ*, 454, L19
- Liu, X.-W. 1998, *MNRAS*, 295, 699
- Liu, X.-W., Storey, P. J., Barlow, M. J., et al. 2000, *MNRAS*, 312, 585
- Liu, X.-W., Luo, S.-G., Barlow, M. J., Danziger, I. J., & Storey, P. J. 2001, *MNRAS*, 327, 141
- Liu, Y., Liu, X.-W., Luo, S.-G., & Barlow, M. J. 2004, *MNRAS*, 353, 1231
- Luo, S.-G., Barlow, M. J., Danziger, I. J., & Storey, P. J. 2001, *MNRAS*, 327, 141
- Luridiana, V., Pérez, E., & Cerviño, M. 2003a, *AJ*, 125, 3196
- Luridiana, V., Peimbert, A., Peimbert, M., & Cerviño, M. 2003b, *ApJ*, 592, 846
- O'Dell, C. R., Peimbert, M., & Peimbert, A. 2003, *AJ*, 125, 2590
- Papaderos, P., Izotov, Y. I., Guseva, N. G., Thuan, T. X., & Fricke, K. J. 2006a, *A&A*, 454, 119
- Papaderos, P., et al. 2006b, in preparation
- Peimbert, A. 2003, *ApJ*, 584, 735
- Peimbert, A., Peimbert, M., & Luridiana, V. 2002, *ApJ*, 565, 668
- Peimbert, M. 1967, *ApJ*, 150, 825
- Peimbert, M., & Torres-Peimbert, S. 1992, *Rev. Mex. Astron. Astrofis.*, 24, 155
- Peimbert, M., Storey, P. J., & Torres-Peimbert, S. 1993, *ApJ*, 414, 626
- Peimbert, M., Torres-Peimbert, S., & Luridiana, V. 1995, *Rev. Mex. Astron. Astrofis.*, 31, 131
- Peimbert, M., Peimbert, A., & Ruiz, M. T. 2000, *ApJ*, 541, 688
- Peimbert, M., Peimbert, A., Ruiz, M. T., & Esteban, C. 2004, *ApJS*, 150, 431
- Pérez, E. 1997, *MNRAS*, 290, 465
- Press, W. H., Teukolsky, S. A., Vetterling, W. T., & Flannery, B. P. 1992, *Numerical Recipes in C, The Art of Scientific Computing /Second Edition/* (Cambridge University Press)
- Rubin, R. H., Bhatt, N. J., Dufour, R. J., et al. 2002, *MNRAS*, 334, 777
- Rubin, R. H., Martin, P. G., Dufour, R. J., et al. 2003, *MNRAS*, 340, 362
- Ruiz, M. T., Peimbert, A., Peimbert, M., & Esteban, C. 2003, *ApJ*, 595, 247
- Shapley, A. E., Steidel, C. C., Pettini, M., Adelberger, K. L., & Erb, D. K. 2006, *ApJ*, 651, 688
- Stasińska, G., & Izotov, Y. I. 2003, *A&A*, 397, 71
- Torres-Peimbert, S., Peimbert, M., & Peña, M. 1990, *A&A*, 233, 540
- Tsamis, Y. G., & Péquignot, D. 2005, *MNRAS*, 364, 687
- Tsamis, Y. G., Barlow, M. J., Liu, X.-W., Storey, P. J., & Danziger, I. J. 2004, *MNRAS*, 353, 953
- Viegas, S., & Clegg, R. E. 1994, *MNRAS*, 271, 993
- Wesson, R., Liu, X.-W., & Barlow, M. J. 2005, *MNRAS*, 362, 424
- Whitford, A. E. 1958, *AJ*, 63, 201
- Zhang, Y., Liu, X.-W., Wesson, R., et al. 2004, *MNRAS*, 351, 935
- Zhang, Y., Liu, X.-W., Liu, Y., & Rubin, R. H. 2005, *MNRAS*, 358, 457

# Online Material

**Table 1.** Journal of the observations.

Name <sup>a</sup>	Data of Obs	Exp <sup>b</sup> (s)	A.M. <sup>c</sup>	Name <sup>a</sup>	Data of Obs	Exp <sup>b</sup> (s)	A.M. <sup>c</sup>
SBS 0335-052E SE	Oct. 9	2700	1.16	J 0113+0052	Oct. 9	3600	1.21
Pox 186	Apr. 14	2400	1.27	J 0133+1342	Oct. 7	3600	1.38
HS 2236+1344a	Oct. 7	3600	1.38	Pox 4b	Apr. 12	3600	1.10
UM 461a	Apr. 12	3600	1.12	IC 4662a	Apr. 13	2100	1.23
J 1044+0353a	Apr. 13	3600	1.19	J 1430+0027	Apr. 12	2400	1.67
Tol 1214-277	Apr. 14	2400	1.09	IC 4662c	Apr. 13	2100	1.23
UM 570	Apr. 11	3600	1.13	Pox 120b	Apr. 13	2700	1.05
CGCG 032-017	Apr. 14	2400	1.24	g2252292-171050	Oct. 9	1200	1.10
Pox 108	Apr. 12	2700	1.47	UM 461b	Apr. 12	3600	1.12
UM 559	Apr. 14	2400	1.24	Mrk 1236c	Apr. 14	1920	1.16
SBS 0335-052E #7	Oct. 7	2400	1.12	J 1448-0110	Apr. 11	3600	1.22
UM 442	Apr. 12	2400	1.18	IC 4662b	Apr. 13	2100	1.23
Mrk 1329	Apr. 12	3600	1.51	J 2230-0006	Oct. 8	3600	1.30
Mrk 1236a	Apr. 14	1920	1.16	Pox 105	Apr. 11	3600	1.20
Tol 2146-391	Apr. 13	2292	1.38	UM 462d	Apr. 14	2400	1.12
CGCG 007-025a	Apr. 12	3600	1.14	UM 462c	Apr. 14	2400	1.12
HS 2134+0400	Oct. 8	3600	1.27	J 0248-0817b	Oct. 7	3600	1.07
J 0014-0043	Oct. 9	2700	1.37	CGCG 007-025b	Apr. 12	3600	1.14
J 2324-0006	Oct. 7	3600	1.15	J 1624-0022	Apr. 11	3600	1.18
SBS 0335-052E #3b	Oct. 9	2700	1.16	UM 462e	Apr. 14	2400	1.12
J 1253-0312	Apr. 13	2700	1.18	J 0134-0038	Oct. 9	2400	1.18
J 1201+0211	Apr. 14	2400	1.21	SBS 0335-052W	Oct. 9	3600	1.10
SBS 0335-052E #3a	Oct. 9	2700	1.16	Tol65b	Apr. 13	3600	1.02
Tol 65a	Apr. 13	3600	1.02	SBS 0335-052 #4,5	Oct. 9	2700	1.16
UM 311	Oct. 8	1800	1.25	UM 462b	Apr. 14	2400	1.12
J 1304-0333	Apr. 13	1800	1.86	CGCG 007-025d	Apr. 12	3600	1.14
J 0248-0817a	Oct. 7	3600	1.07	ESO 338-IG04	Apr. 12	1228	1.05
Pox 4a	Apr. 12	3600	1.10	Mrk 1236b	Apr. 14	1920	1.16
Pox 120a	Apr. 13	2700	1.05	J1414-0208	Apr. 13	3600	1.16
HS 2236+1344b	Oct. 7	3600	1.38	IC 4662d	Apr. 13	2100	1.23
CGCG 007-025c	Apr. 12	3600	1.14	J 0107+0103	Oct. 8	3200	1.17
UM 462a	Apr. 14	2400	1.12	g0405204-364859	Oct. 8	2400	1.03
J 2302+0049	Oct. 8	2400	1.16	J 1044+0353b	Apr. 13	3600	1.19
Tol2138-405	Apr. 14	2260	1.35	IC 4662e	Apr. 13	2100	1.23
J 2104-0035N	Oct. 8	3600	1.16				

<sup>a</sup> Names of the SDSS objects are given abridged without seconds. <sup>b</sup> Total exposure time. <sup>c</sup> Air mass at the beginning of the observation.

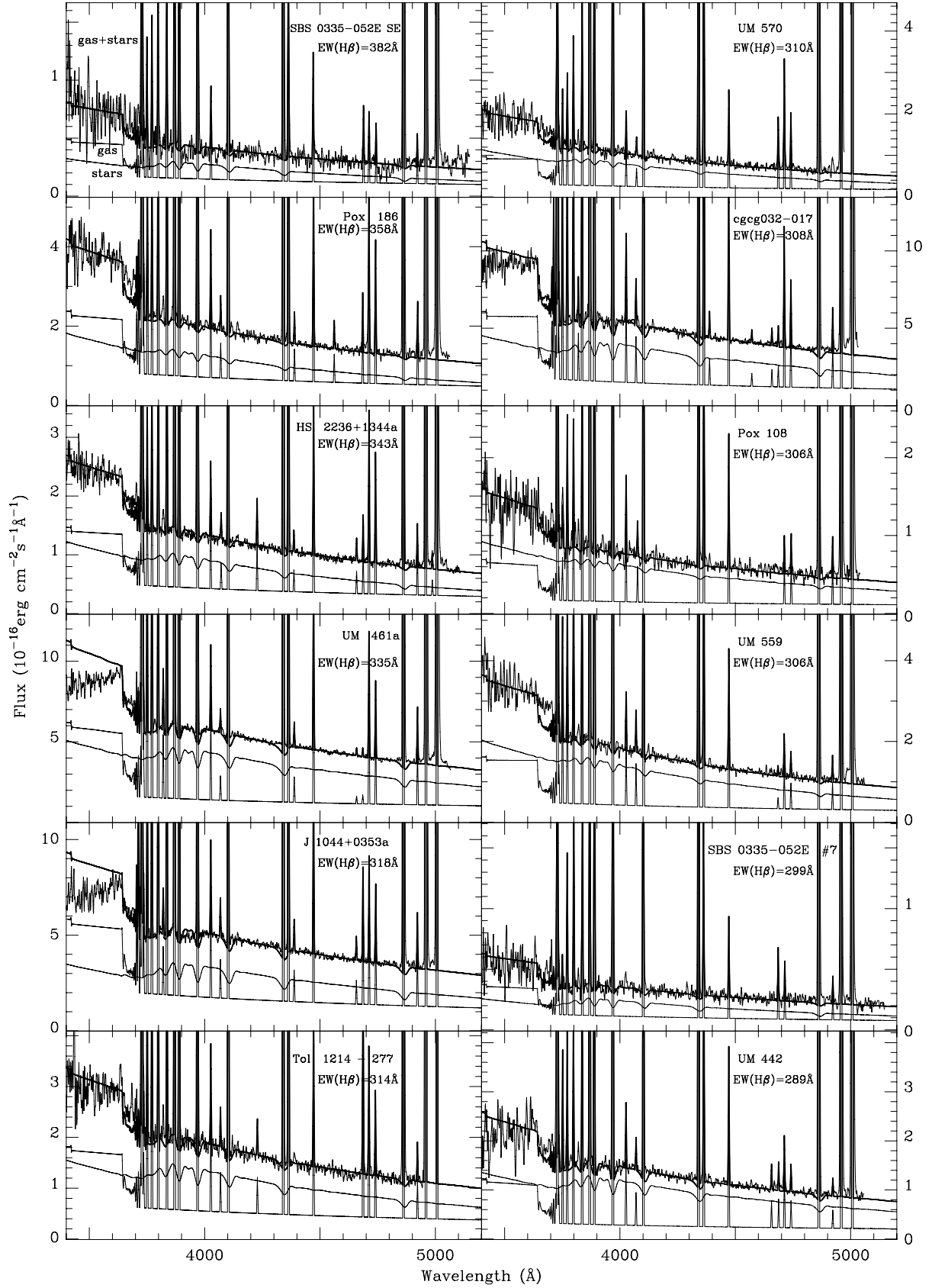


**Fig. 3.** Best fit model SEDs (thick solid lines) superposed by the redshift- and extinction-corrected 3.6 m spectra of 69 H II regions in 45 blue compact dwarf galaxies. The separate contributions from the stellar and ionised gas components are shown by thin solid lines (see the labels in the upper left panel of each page). Names of the SDSS objects are given in short form without seconds.

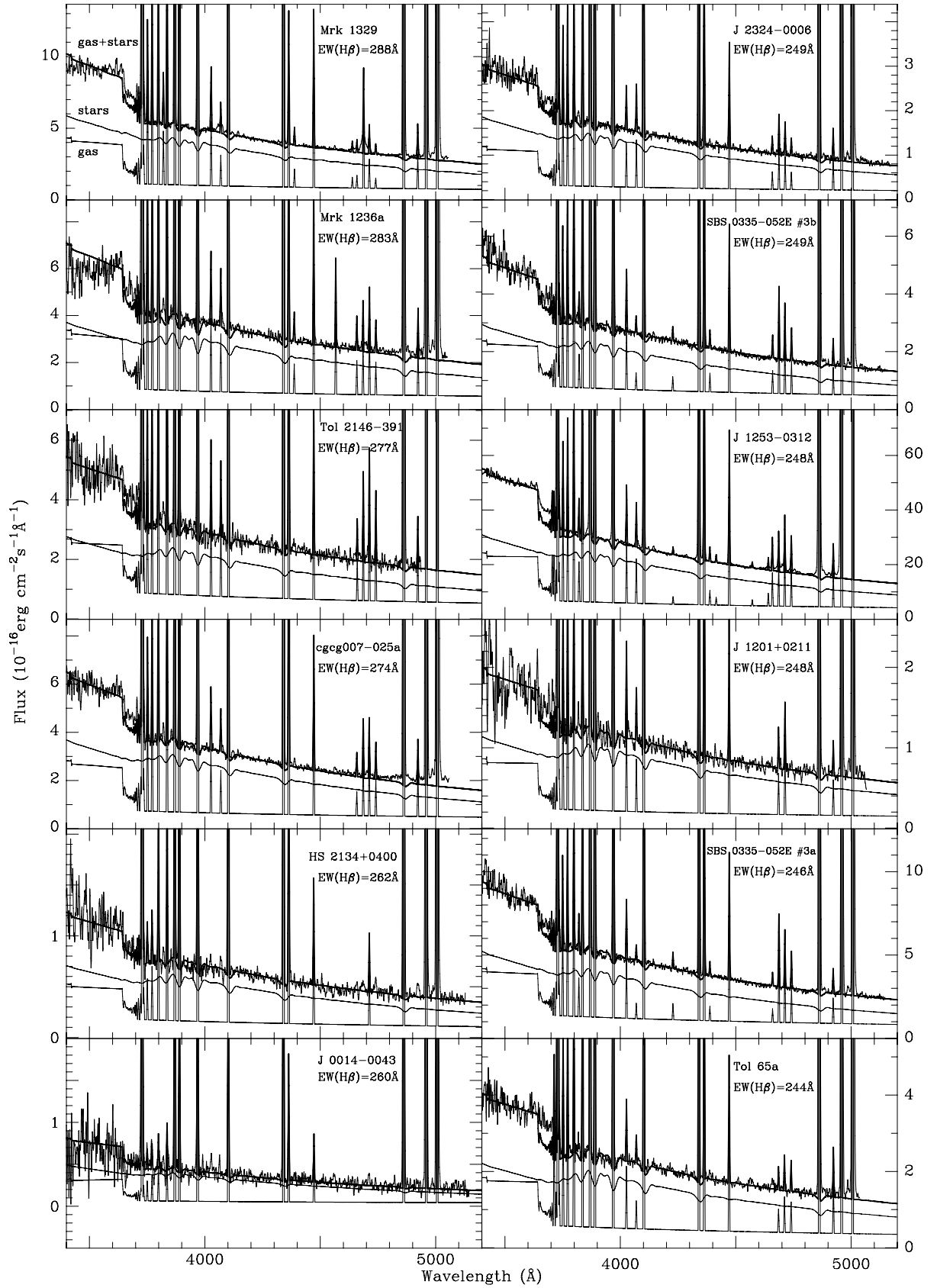


Fig. 3. continued.

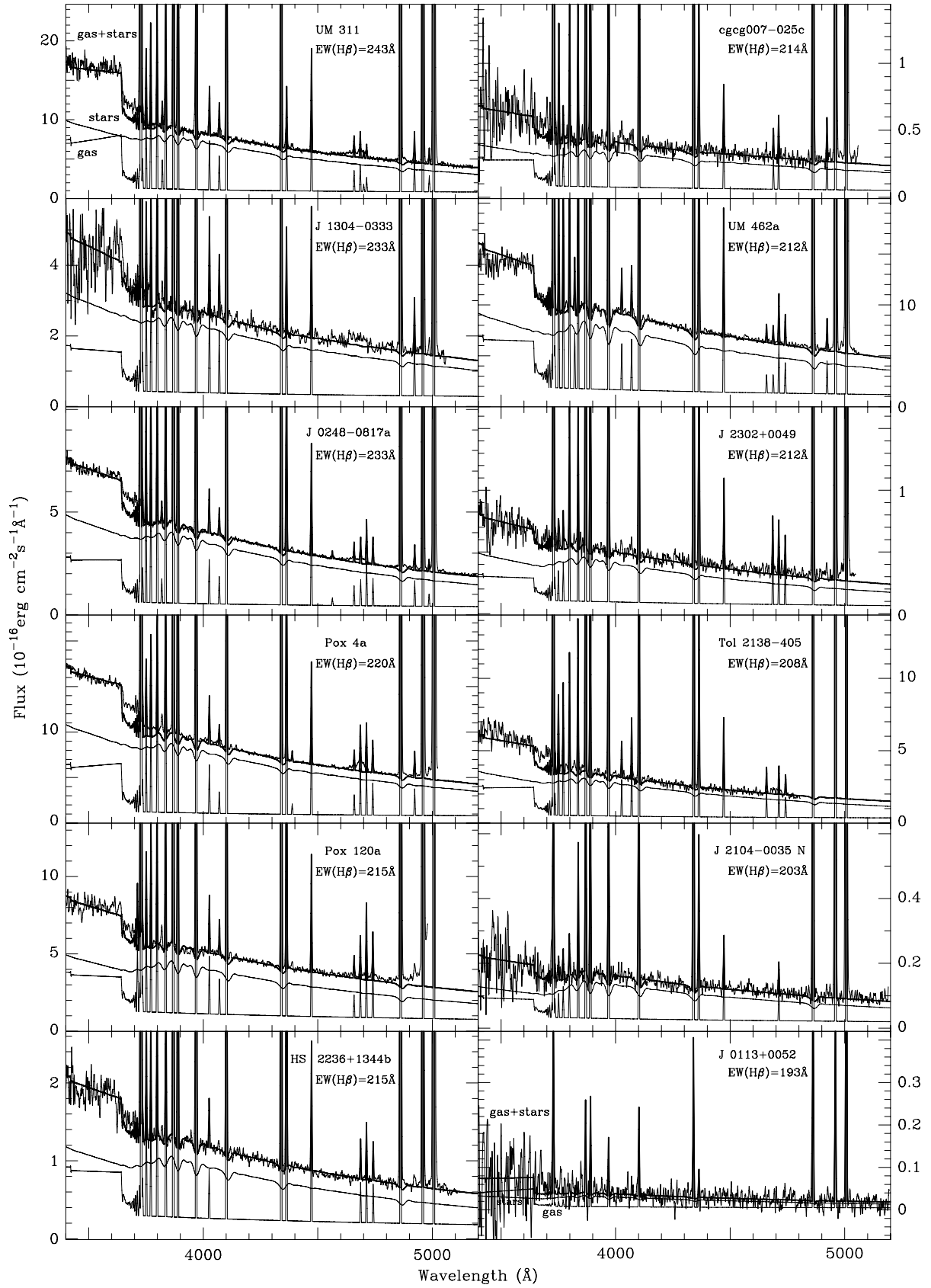


Fig. 3. continued.

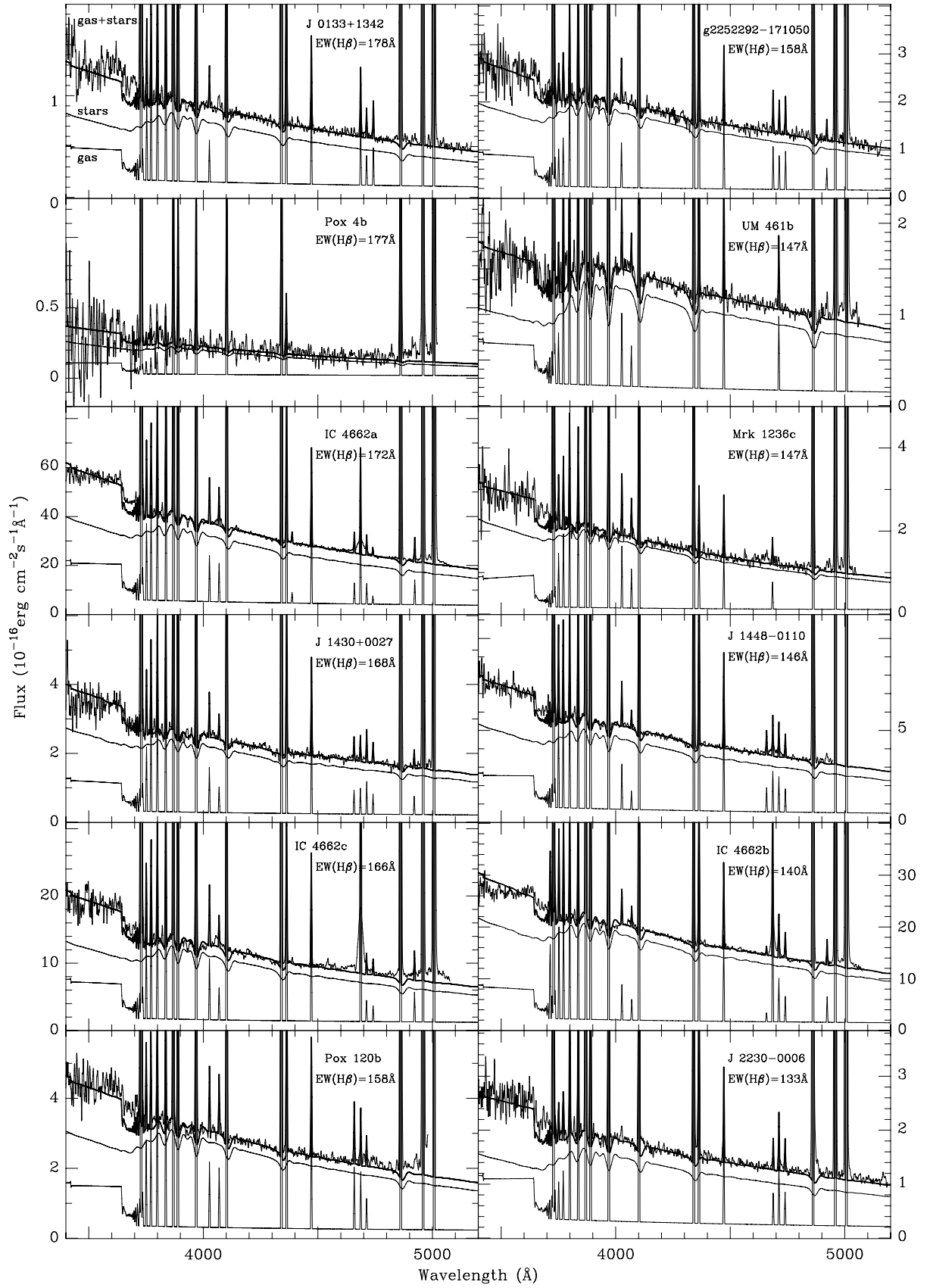


Fig. 3. continued.

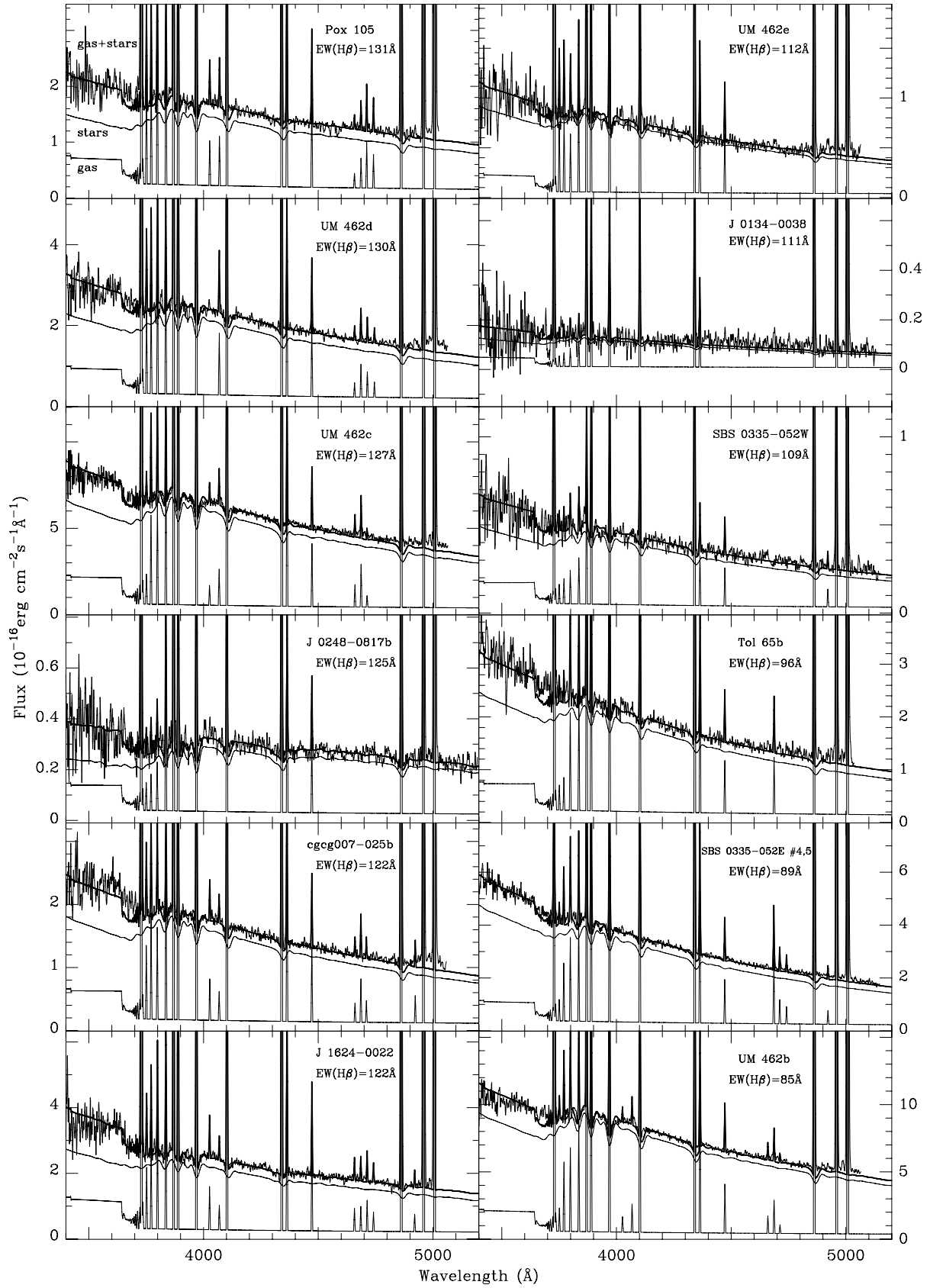


Fig. 3. continued.

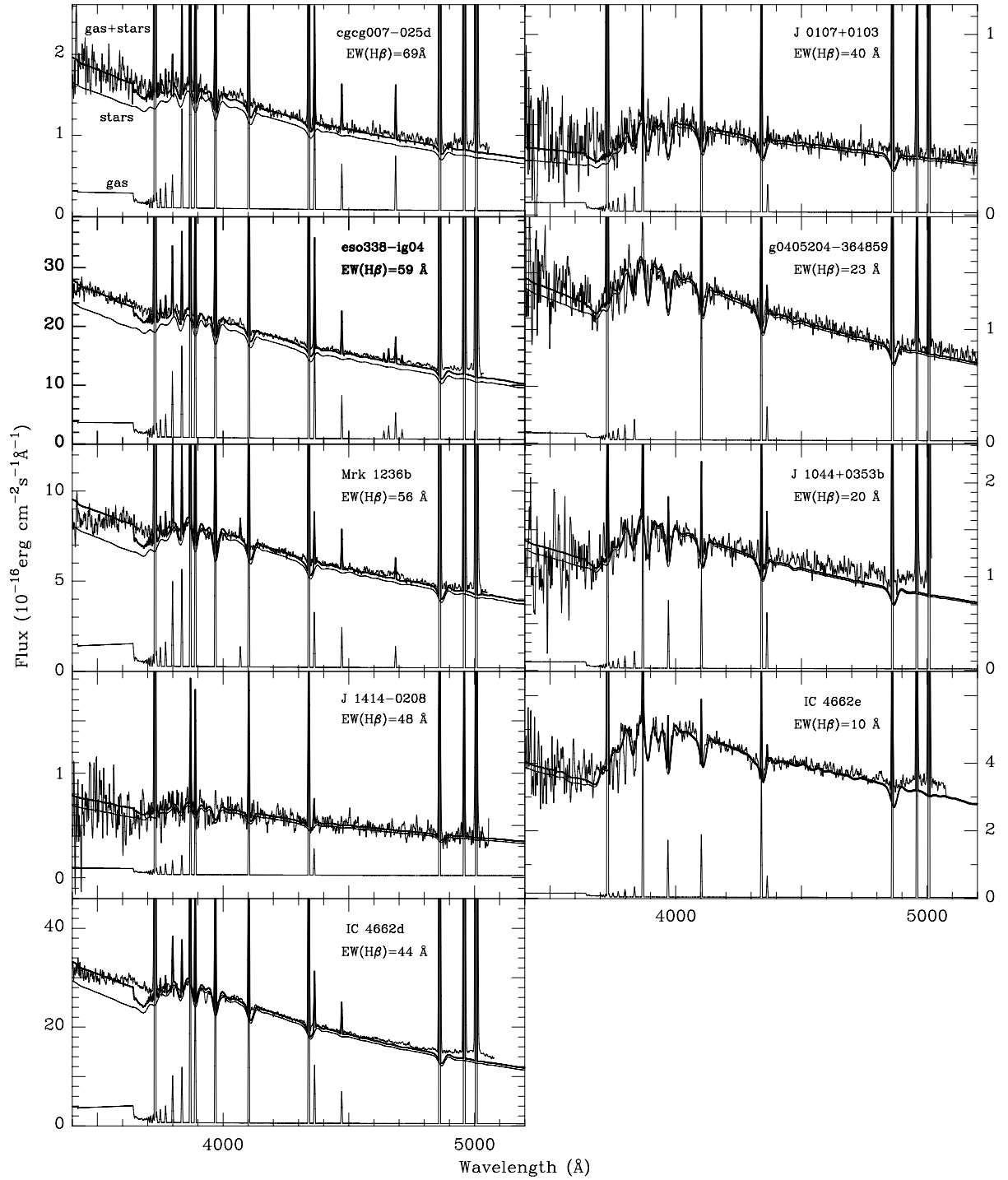


Fig. 3. continued.